The multiplexed chemical kinetic photoionization mass spectrometer: a new approach to isomer-resolved chemical kinetics.

David L. Osborn,[*†] Peng Zou,[*] Howard Johnsen,[*] Carl C. Hayden,[*] Craig A. Taatjes,[*†] Vadim D. Knyazev,[‡] Simon W. North,[§] Darcy S. Peterka,[**] Musahid Ahmed,[**] and Stephen R. Leone[**††]

Contribution from the Combustion Research Facility, Mail Stop 9055, Sandia National Laboratories, Livermore, California 94551-0969, Research Center for Chemical Kinetics, Department of Chemistry, The Catholic University of America, Washington, DC 20064, Department of Chemistry, Texas A&M University, PO Box 30012, College Station, Texas, 77842, and Chemical Sciences Division, Ernest Orlando Lawrence Berkeley National Laboratory, Berkeley, California 94720, Departments of Chemistry and Physics, University of California, Berkeley, California 94720

Electronic mail: dlosbor@sandia.gov (DLO), cataatj@sandia.gov (CAT).

We have developed a multiplexed time- and photon-energy–resolved photoionization mass spectrometer for the study of the kinetics and isomeric product branching of gas phase, neutral chemical reactions. The instrument utilizes a side-sampled flow tube reactor, continuously tunable synchrotron radiation for photoionization, a multi-mass double-focusing mass spectrometer with 100% duty cycle, and a time- and position-sensitive detector for single ion counting. This approach enables multiplexed, universal detection of molecules with high sensitivity and selectivity. In addition to measurement of rate coefficients as a function of temperature and pressure, different structural isomers can be distinguished based on their photoionization efficiency curves, providing a more detailed probe of reaction mechanisms. The multiplexed 3-dimensional data structure (intensity as a function of molecular mass, reaction time, and photoionization energy) provides insights that might not be available in serial acquisition, as well as additional constraints on data interpretation.

---

[*] Sandia National Laboratories
[†] Authors to whom correspondence should be addressed.
[‡] The Catholic University of America
[§] Texas A & M University
[**] Ernest Orlando Lawrence Berkeley National Laboratory.
[††] University of California, Berkeley

I. INTRODUCTION

Chemical kinetics, the study of rates and underlying mechanisms of chemical reactions, plays a fundamental role in our understanding of chemistry. Since the pioneering research of Wilhelmy[1] on the rate of hydrolysis of sucrose, chemists have pursued new experimental methods to measure the time evolution of reactions with greater selectivity and sensitivity. In the field of gas phase reactions, the flash photolysis technique developed by Porter and Norrish[2] provided sufficient time resolution and selectivity to measure the concentration of transient species. The ability to observe these reaction intermediates has greatly advanced our ability to test chemical reaction mechanisms.

Although gas phase chemical kinetics is well established, significant challenges remain that can be addressed with new experimental capabilities. Two problems of great importance that have been difficult to unravel are the isomeric nature of reaction products and the study of interlinked sets of reactions. In this paper we describe a new experimental apparatus capable of addressing these and other contemporary problems in the study of reaction mechanisms.

To frame the challenge, we propose ideal capabilities of a chemical kinetics experimental apparatus suited to detection of neutral reactants, intermediates, and products. An ideal detection strategy should be universal (applicable to all atoms and molecules), multiplexed (detecting all species simultaneously), selective (resolving each structural isomer of each species), and sensitive (detecting low species concentrations). Furthermore, the temperature and pressure in the reactor should be variable over a wide range to explore how thermal energy and collisions reveal the shape of the potential

energy surface. Finally, the technique should have sufficient temporal resolution to measure rate coefficients spanning several orders of magnitude.

Our apparatus, consisting of a side-sampled flow tube reactor, flash photolysis initiation of reactions, and synchrotron photoionization mass spectrometry has the potential to meet all of these goals. Because all neutral atoms and molecules can be ionized, mass spectrometry is in principle a truly universal technique, and in practice nearly so. Multiplexed detection of a wide range of masses is possible with many mass spectrometric instruments, including sector, time-of-flight, ion cyclotron, and ion trap spectrometers. Mass spectrometers are inherently selective by sorting species according to their mass-to-charge (m/z) ratio. Finally, the ability to detect single ions against nearly zero background makes mass spectrometry highly sensitive.

However, conventional electron bombardment ionization of neutrals, using electrons with 70 eV kinetic energy, suffers from two main drawbacks. First, significant fragmentation occurs during ionization, so that a single neutral species produces cations at the parent mass and many lighter fragment masses, leading to complex mass spectra. Fragmentation occurs because the incident electron provides sufficient energy to both ionize the neutral and break chemical bonds in the resulting cation. Second, although different structural isomers in general have distinct fragmentation patterns that can provide secure structural assignments, a complex mixture of species generates many overlapping fragmentation patterns, from which a unique determination of the mixture composition is generally not possible.[3] Both drawbacks can be avoided by ionizing a molecule within a few electron volts of its ionization energy (IE).

To distinguish each structural isomer, we take advantage of the fact that different structural isomers of the same *m*/*z* ratio (for example, allene (H_2CCCH_2) and propyne ($HCCCH_3$)) in general have different photoionization efficiency (PIE) spectra (ion yield vs. excitation energy). In particular, the PIE curve of each isomer generally has a distinct IE (threshold for ionization), shape (determined by Franck-Condon overlap of the neutral with the cation), and intensity (ionization cross section).

Although several groups have succeeded in implementing low-energy, tunable electron-bombardment ionization,[4] the low flux and poor energy resolution of the electron beam leads to reduced sensitivity and selectivity compared to photoionization. The historical disadvantage of single-photon photoionization is the difficulty of making vacuum ultraviolet photons in the 6.5 – 16 eV range that are simultaneously intense, widely tunable, spectrally narrow, and of high duty cycle. The development of modern synchrotron radiation has largely eliminated this disadvantage, and is a key component in the success of the present apparatus.

Our instrument's design is inspired by the successful photoionization mass spectrometer (PIMS) of Slagle and Gutman,[5,6] which uses fixed-frequency VUV radiation from microwave discharge lamps to form photoions that are analyzed with a quadrupole mass spectrometer. Conceptually, we have made two major modifications to their approach. First, our photoionization method utilizes radiation from the Chemical Dynamics Beamline of the Advanced Light Source (ALS) Synchrotron of Lawrence Berkeley National Laboratory. This third-generation synchrotron can produce widely tunable (7.2 – 25 eV), high brightness (10^{21} photons cm^{-2} sr^{-1}), medium resolution ($E/\Delta E$ ~ 1000) VUV radiation. The high brightness of this source enables high sensitivity,

whereas the narrow bandwidth and broad tunability provides high selectivity, allowing one to minimize or eliminate fragmentation while sorting different structural isomers by virtue of their different IEs.

The second innovation is the use of a multiplexed mass spectrometer in order to detect multiple masses simultaneously with 100% duty cycle. Multiplexed detection is not only more efficient, it also has benefits in reducing systematic errors due to drifts in experimental parameters with time. Two other implementations of multiplexed mass spectrometers applied to the general PIMS design of Slagle and Gutman have appeared in the literature, by Fockenberg *et al*.[7] and Blitz *et al*.[8] Both of these instruments utilize pulsed-extraction time-of-flight mass spectrometers, coupled with either a continuous hollow cathode discharge lamp[7] or a pulsed frequency-tripled laser[8] to provide VUV photons.

Chemical reactions occur in a variable temperature (300 – 1000 K) and pressure (1 – 10 Torr) flow tube reactor. We use pulsed-laser photolysis of precursor molecules to create uniform densities of reactive free radicals on a timescale short compared to their reactive decay. To maximize the efficiency of data collection, molecules should be detected in a continuous fashion, beginning before the radical-generating laser pulse and continuing until chemical reactions have run their course. Reaching this goal requires both a continuous (i.e., not pulsed) photon source and a continuous mass spectrometer. In fact neither the photons nor the mass spectrometer need be truly continuous, but if pulsed, they should have a repetition rate greater than the desired detection bandwidth. The quasi-continuous nature of the ALS radiation led to our selection of a miniature double-focusing sector mass spectrometer[9] of the Mattauch-Herzog[10] geometry for

multiplexed mass detection. This spectrometer provides 100% duty cycle and a straightforward separation of the mass resolution from temporal (kinetic) resolution.

Our multiplexed, time-resolved photoionization mass spectrometer produces 3-dimensional data sets that provide an unusual level of detail in the study of gas phase chemical reactions. The data can be represented as the function $S(m/z, t, E)$, where S is proportional to the concentration of neutrals molecules in the chemical reactor as a function of mass-to-charge ratio of the detected ion, reaction time, and photoionization energy. These data provide multiple "images" of the chemical reactions under study,[11] yielding both rate coefficients and isomer-resolved product branching ratios as a function of temperature and pressure. In this paper we present a detailed description of the apparatus, together with results that demonstrate its usefulness in solving contemporary problems in chemical kinetics. Several studies using the apparatus have already appeared.[11-14]

II. EXPERIMENT

The experimental apparatus comprises four main sections: A) the chemical reactor and vacuum system, B) the photoionization source, C) the mass spectrometer, and D) the ion detector and data acquisition system. Each section will be described in detail below.

A. Chemical reactor and vacuum system

A cross section view of the multiplexed photoionization mass spectrometer is shown in Fig. 1, with a magnified view of the central portion shown in Fig. 2. The component gases flowing into the 62 cm long quartz reactor tube (1.27 cm outer diameter, 1.05 cm inner diameter) are metered by individual, calibrated mass flow controllers. The pressure in the reactor tube is measured with a capacitive manometer and controlled with a closed-

loop feedback valve throttling the Roots pump that removes the majority of gases from the reactor. From a pinhole (650 μm or 400 μm diameter) in the side of the reactor tube a sample of the gas mixture emerges into the source chamber, forming a molecular beam characterized by gas dynamics that are neither purely effusive nor fully supersonic. The source chamber is evacuated by a 3200 L s^{-1} oil-free turbomolecular pump. The molecular beam is skimmed 0.2 – 0.3 cm downstream from the pinhole by a 0.15 cm diameter skimmer before entering the differentially-pumped ionization chamber.

It is important to differentiate the side-sampled, slow-flow reactor in this work from end-sampled, fast-flow reactors[15,16] common in gas phase chemical kinetics. In our slow-flow reactor, we create an initial distribution of radicals that becomes both radially and axially homogenous on a timescale short compared to the bimolecular kinetics under study. As a result, the time-dependent concentration changes due to chemical reactions are independent of the radial and axial position from which a sample is extracted, and therefore accurate measurement of the bulk flow velocity is not required. By contrast, in the fast-flow technique, the radical species is added to the flow using a moveable injector at a series of i discrete axial positions d_i, where d_i is the distance along the tube centerline between the injector and the sampling orifice. In this case the time-dependent species concentrations are converted into a spatial dependence, and it is therefore important to measure the bulk flow velocity accurately. In both designs, all species (including free radicals) will have many collisions with the walls of the reactor before emerging through the sampling orifice. The inner surface of the flow tube must therefore be made sufficiently inert that first-order radical loss on the reactor walls is slower than loss by gas phase reactions.

The typical gas mixture entering the reactor tube consists of a radical precursor and an excess reactant diluted in helium. The quartz reactor tube is wrapped with 18 μm thick nichrome tape for resistive heating of the reactor tube over a 39 cm length beginning 23 cm upstream from the pinhole. The heating tape is wrapped with a layer of insulating square-weave, yttria-stabilized zirconia cloth (ZYW-15, Zircar Zirconia, Inc.) that is surrounded by the two halves of a gold-plated copper sheath. These layers around the reactor tube serve multiple purposes: preventing short circuits in successive turns of the heating tape, increasing temperature uniformity along the tube length, and reducing radiative heat transfer from the tube to the vacuum chamber. The temperature in the reactor is monitored by a thermocouple on the centerline of the reactor, 3 cm downstream from the pinhole. This reading is used in a closed-loop feedback circuit to regulate the gas temperature over the range 300 – 1050 K. The temperature uniformity at 1023K is ± 4 K measured from 8 cm before to 7 cm after the pinhole.

Free radicals are generated by photodissociation of precursor molecules with an unfocused excimer laser pulse (fluence = 10 – 60 mJ cm^{-2}, pulsewidth = 20 ns, wavelength = 193 nm, 248 nm, or 351 nm) propagating collinearly down the reactor tube. At each pressure and temperature, the total gas flow rate is adjusted to maintain a flow velocity of ~ 400 cm s^{-1}. At a laser repetition rate of 4 Hz, these conditions provide a fresh sample of gas for each laser pulse. The portion of the excimer laser beam that propagates down the reactor tube is not perfectly uniform. In practice, this inhomogeneity is minor if the laser is well-aligned through the tube. Furthermore, in order to assure radially-uniform initial radical density, the total pressure is kept low so that gaseous diffusion smoothes any inhomogeneity on a timescale short compared to the

pseudo first-order reaction rate under study. Axial homogeneity is achieved by maintaining sufficiently low densities of the radical precursor such that the laser intensity change due to absorption is negligible along the length of the reactor tube. In a bath gas of helium, the required homogeneity of radical density is observed at least over the pressure range of 1 – 10 Torr.

The remainder of the vacuum system consists of two turbomolecular pumps, of pumping speeds 1600 L s^{-1} and 700 L s^{-1}, that evacuate the ionization region and the detector region, respectively (Figs 1 and 2). The turbomolecular pumps are backed by oil-free scroll pumps.

B. Photoionization source

Our approach of pulsed initiation of reactions with continuous probing requires the use of continuous ionization sources. The apparatus utilizes two complementary radiation sources: either a hollow-cathode discharge lamp or synchrotron radiation from the Chemical Dynamics Beamline of the Advanced Light Source at Lawrence Berkeley National Laboratory. The discharge lamp is comparatively inexpensive and can be used for an indefinite period of time, but produces only a handful of discrete photon energies from discharges in H_2 or the noble gases. By contrast, synchrotron radiation is continuously and rapidly tunable with high brightness, but is only available to us for small time periods each year. The two sources have comparable photon flux at an energy of 10.2 eV.

The third-generation ALS synchrotron extracts VUV radiation (7.2 – 25 eV), from a 1.9 GeV electron storage ring using a 10 cm period undulator, producing a nominal flux of 10^{16} photons s^{-1} with a 2.5% bandwidth.[17] The radiation passes through a windowless

absorption cell filled with 30 Torr of either Ar or Kr to remove harmonics of the undulator radiation with energies above the IEs of these gases. This filtered undulator radiation is dispersed vertically with a 3 m off-plane Eagle monochromator to achieve narrower spectral bandwidth (10 – 50 meV) at the expense of photon flux (~ 10^{13} – 10^{14} photons s^{-1}). After passing through the exit slits of the monochromator, the radiation intersects the molecular beam perpendicularly, 2.5 cm downstream from the pinhole, inside the ionization region of a double-focusing mass spectrometer. The combination of the gas filter and the grating allows us to use a completely windowless path for the ionizing photons from the synchrotron to the mass spectrometer. Although the ALS radiation is pulsed, with a 500 MHz repetition rate, our detection bandwidth is more than an order of magnitude smaller, rendering the radiation quasi-continuous in our apparatus.

The characteristics of the ALS photons enable high sensitivity and high selectivity, allowing one to minimize or eliminate fragmentation while sorting different structural isomers by virtue of their different IEs. The photon energy and bandwidth (50 meV for 600 μm exit slit width) are calibrated by measurement of known atomic resonances of Xe, absorption resonances of Ar (using the gas filter as an absorption cell), and narrow autoionization resonances in O_2. We utilize the discharge lamp for kinetics experiments where extensive signal averaging is necessary and the tunability of the synchrotron is not required. A 0.17 cm inner diameter quartz capillary guides light from the discharge. The capillary ends 1.5 cm from the ionization point. We often use 1 mm thick windows of MgF_2 or LiF to absorb higher energy photons emitted by the discharge lamp.

C. Mass spectrometer

The goal to continuously probe reactants and products simultaneously over a wide range of masses led to the selection of a miniature double-focusing sector mass spectrometer (Fig. 2) of the Mattauch-Herzog geometry.[9] This spectrometer has only DC electric fields, providing 100% duty cycle and a straightforward separation of the mass resolution from temporal (kinetic) resolution. The detector, power supplies, and control electronics were purchased from Intelligent Ion (now OI Analytical). The ion optics were redesigned for compatibility with photoionization.

After acceleration, the ions are dispersed by kinetic energy in the electrostatic sector. The central section of the ion beam (with narrower kinetic energy spread) passes through a slit into the magnetic sector (0.94 T permanent magnetic field), where the ions are spatially dispersed according to the square root of their mass. The ions come to a focus in the plane of dispersion at the exit face of the magnet, with a potential energy of 0 V. In the Mattauch-Herzog geometry, for any ion *i*, the relationship between the spatial position x_i (cm) along the x-axis of the detector to mass m_i (amu) is given by:

$$x_i = \sqrt{2}R = \sqrt{2}\frac{0.0144}{Bz}\sqrt{m_i E_k} \qquad (1)$$

where R (cm) is the radius of curvature of ions with kinetic energy E_k (eV) and charge $+z$ in a magnetic field B (T).

The overall length of the mass spectrometer is on the order of 7.5 cm, significantly smaller in size and weight than most sector mass spectrometers. Mass resolution will be discussed in section III.A.

D. Ion Detector and data acquisition system

At the exit face of the magnet, all ions within a variable mass range of ~8 × (e.g., m/z = 14 – 112) strike the active area of a time- and position-sensitive microchannel plate detector with a delay-line anode.[18] A side view of the detector, constructed of non-magnetic materials, is shown schematically in Fig. 3. The ions pass through an electroformed gold mesh (period 101.6 μm in x and y dimensions) held at ground potential. After passing through the mesh, the ions are accelerated by a negative potential (-4400 – -5400 V) applied to the first of three optical-quality, impedance-matched microchannel plates (MCP). The third MCP is driven into saturation, producing a total gain of ~ 2 x 10^7 electrons for each incident cation. The electron cloud is accelerated by a ~700 V potential toward a 65 ns long, 2-D delay-line anode held at ground. The plan view of the anode is shown schematically in Fig. 3.

The background count rate over the 1 x 4.5 cm^2 active area of the detector is typically < 10 s^{-1} with the mass spectrometer on but without VUV radiation. Spatial resolution of the detector is ~ 40 μm as measured by the shadow of the gold grounding mesh when the detector is illuminated with 253 nm plane wave radiation.

The position of a single ion's impact on the first microchannel plate determines the centroid of the electron cloud impinging on the conductive fingers of the x and y layers of the anode. These fingers are connected to serpentine delay lines as shown in Fig. 3. The ion position is measured by the differential time required for the ~ 3 pC pulse of electrons to propagate to opposite ends of the x and y delay lines. After amplification, the pulses pass through constant fraction discriminators (to increase the fidelity of their timing information) and enter the "start" and "stop" inputs of a time to digital converter (TDC). The TDC converts the time delays to14-bit digital numbers that are proportional to the

ion's impact coordinates. The x coordinate determined is proportional to $(m/z)^{0.5}$ of the incident ion. The extra delay added to one end of each delay line ensures that the stop input always arrives after the start input, regardless of the ion impact position.

If valid start and stop pulses are received on the x and y delay lines, a 20 MHz oscillator on a custom-made timestamping board (TS) creates a 32-bit number that represents the ion's time of arrival with respect to the beginning of a single data acquisition cycle. Typically, each cycle begins 20 ms before the laser pulse and lasts 150 ms. The two 14-bit numbers representing the ion's x and y coordinates are interleaved with the 32-bit time value and transferred to a dynamic memory access (DMA) card in the data acquisition computer. Custom software written in LabView triggers both the DMA card and the delay generator that precisely controls the timing of the excimer laser pulse generating free radicals. The timing jitter between successive data cycles is negligible compared to the temporal instrument response function that is determined by gas dynamics (see section III.D.).

The position and time of arrival with respect to the photodissociation laser is recorded for each ion observed in a single data cycle (containing one laser pulse). The raw data that is periodically written to the computer's hard drive during data collection consists of an (x, y, t) triplet describing each detected ion. This raw data may be filtered and binned in a variety of ways during post-processing in order to extract desired experimental observables. Successive cycles may be coadded to improve the signal-to-noise ratio. Once an ion detection cycle has begun, the TDCs cannot detect another ion for approximately 1 μs. Average ion count rates are restricted to < 30 kHz to ensure linear response.

Time-independent signals may be removed by subtracting, at each bin in the m/z dimension, the average signal taken before the photodissociation laser is fired. Finally, the background-subtracted signal at each photon energy is normalized for the ALS photon flux, as measured by a calibrated, VUV-sensitive photodiode.

III. RESULTS

In this section we describe the performance of the instrument and the new insights these capabilities offer for addressing contemporary problems in chemical kinetics. The performance of the mass spectrometer will be described first, followed by an illustration of the multi-dimensional nature of the data.

A. Time-independent mass spectrometry

The performance of the mass spectrometer can be evaluated in a time-independent measurement (i.e., without the photolysis laser) in which a mixture containing 0.01% each of C_2H_4 and C_3H_6 in helium flows through the reactor tube at a total pressure of 4 Torr. The raw 2-D spatial image of the ions created with radiation from a helium discharge lamp ($E \sim 21.22$ eV) is shown in Fig. 4a. In addition to the parent $C_3H_6^+$ peak at $m/z = 42$, the high photon energy causes extensive dissociative ionization, producing masses 41, 40, 39, and 38. Because the ions are mass dispersed only along the x direction, the image should consist of parallel vertical lines, one for each m/z ratio detected. The actual image shows approximately parabolic curvature of the ion stripes. This artifact appears to arise from fringing fields of the permanent magnet that protrude into the detector.

Periodic variation in ion intensity is also visible in Fig. 4a in both the x and y dimensions. The positions of low-intensity match the orthogonal pattern of the gold

mesh in front of the MCP stack: ions impacting the gold mesh do not reach the MCPs and are not detected. Careful examination of vertical shadow lines in Fig. 4a shows that they are curved in nearly the same fashion as the vertical ion stripes. This observation implies that the ions comprise linear stripes when they pass through the mesh (acquiring a shadow pattern), and are later distorted into a curved shape. It is unlikely that this distortion occurs to the cations themselves, because they are relatively heavy and are accelerated by an ~ -5 kV potential between the mesh and the first MCP. It is more likely that the distortion occurs as the lighter electrons travel from the third MCP to the anode under a smaller accelerating field.

Because the degree of curvature in Fig. 4a varies slowly in the x direction (i.e., the m/z direction), each row of the data can be shifted in the x direction to correct for this artifact, as demonstrated in Fig. 4b. Note that although the y dimension contains no information related to a desired observable, the ability to acquire a complete XY image allows the detection, and correction, of such artifacts, compared with a 1-D array detector method. Summing the data over the y dimension yields the mass spectra shown in Fig. 4c. The mass resolution ($m/\Delta m$, FWHM) increases from ~ 85 in the uncorrected data to ~165 in the corrected data. Under our conditions the overall mass resolution is not limited by the spatial resolution of the detector.

The mass spectrum is calibrated with a standard mixture of equal parts CH_4, C_2H_4, C_3H_6, 1-C_4H_8, Kr, and Xe. These gases provide a wide range of masses (16 – 136 amu) and ionization energies (9.55 – 14.00 eV).

B. Three-dimensional time-resolved mass spectrometry

When the photolysis laser is used to create a population of free radicals inside the reactor tube, the chemical composition of the gas mixture evolves in time. The raw data stream is most generally represented as table of individual ions, described by their position (hence m/z ratio), detection time (50 ns accuracy), and the VUV photon energy that created the ion. The full mass and time range are acquired simultaneously on each laser pulse, typically with 200 – 500 pulses at each photon energy E. The photon energy is incremented (typically by 25 meV) and the process repeated until the desired photon energy range is covered. In order to extract useful observables, the raw data are binned into a 3-D data cube $S(m/z, t, E)$ in which the user defines the size of the bins in each dimension.

A representation of a 3-D data cube is illustrated in the center of Fig. 5. Unfortunately, a 3-D representation of actual data is difficult to visualize. Therefore, data analysis usually consists of slicing the 3-D data into various 2-D images, from which further slicing into 1-D plots yields data used for quantitative comparisons.

The data in Fig. 5 show photolysis of propargyl chloride (C_3H_3Cl) at 193 nm, and the subsequent reactions that ensue. From a kinetics viewpoint, the most intuitive way to slice the 3-D data cube is to plot an image of intensity as a function of reaction time and mass at one photon energy (upper right image in Fig. 5). This image, at E = 10.2 eV, shows several weak signals that are time-independent, along with 7 intense m/z channels that are laser initiated. The 1-D plots of the time-dependence of m/z = 39 and 78 confirm that C_3H_3 is a photolytically-produced reactant, whereas C_6H_6 is a reaction product of the $C_3H_3 + C_3H_3$ reaction.

The (t, m/z) image provides at a glance a global picture of the time-dependence of the reaction system, and it can also be sliced horizontally to provide a complete 1-D mass spectrum at any time. Compared to an experiment that collects either time or mass data sequentially, the multiplexed nature of our method reduces the probability that drifts in experimental parameters will lead to systematic errors. Furthermore, the multi-mass capability may reveal unexpected mass channels.

Another illuminating way to slice the 3-D data is to plot intensity as a function of VUV photon energy and mass (E, m/z), as shown in the upper left image of Fig. 5, summed over a time window of 0 – 60 ms. The principal value of this image is to reveal the isomeric composition of molecules at each m/z ratio. As discussed in the introduction, a neutral molecule's photoionization efficiency (PIE) as a function of energy is, in general, distinct for each structural isomer, because the threshold ionization energy, shape, and intensity of the PIE curve depends on both the nuclear and electronic configuration of each isomer.

For example, a 1-D plot of the PIE curve observed from m/z = 39, shown in the top left of Fig. 5, has a threshold at 8.67 eV,[19] and a shape that agrees well with the known PIE curve[20] of the propargyl isomer (CH_2CCH) of the C_3H_3 radical. The autoionizing resonances at 9.25, 9.4, and 9.6 eV provide further evidence for the assignment to the propargyl radical. By contrast, the PIE curve of m/z = 78 is not that of a single structural isomer of C_6H_6. The analysis of this PIE curve shows definitive evidence for the C_6H_6 isomers fulvene and 1,5-hexadiyne, among other isomers.[21]

The final orthogonal 2-D slice to take from the 3-D data cube is intensity as a function of photon energy and reaction time for a selected mass. The lower left of Fig. 5

shows such an (E, t) image for m/z = 39, with extracted 1-D plots at 9.2 and 10.3 eV shown in the lower right. When observed with E = 9.2 eV photons, the time profile of cations at m/z = 39 behave in a plausible manner: a sudden rise from photolysis of propargyl chloride, and a decay to zero intensity at long time, as expected for a reactive free radical.

By contrast, using 10.3 eV photons leads to a time profile that is qualitatively similar, but does not decay to zero intensity at 80 ms reaction time. From this behavior we conclude that a small portion of the m/z = 39 cations do not arise from ionization of mass 39 neutrals, but rather from dissociative ionization of a larger, closed-shell species with a daughter ion at m/z = 39. Stated differently, if the time profile of a particular m/z is not independent of photon energy, either multiple isomers with different reactivities are present, or the ionization process is producing cations at one mass from neutrals at multiple masses. In either case, the (E, t) slice reveals useful information that is not readily available from the other two slice directions, providing further constraints on interpretation of the data.

It should be emphasized that Fig. 5 shows only one particular set of 2-D slices from the 3-D data. Choosing different values for the dimension not plotted in a 2-D image (for example, the temporal dimension in the (E, m/z) image) can reveal critical insights into the chemical reaction mechanism under study. As an example, in the CH + C_2H_2 → C_3H_2 + H reaction, we find that different isomers of the C_3H_2 product react at different rates.[22] Specifically, we observe that the triplet propargylene isomer (HCCCH, IE = 8.96 eV) reacts 4 times faster than the cyclic cyclopropenylidene isomer (c-C_3H_2, IE = 9.15

eV). We can obtain this result cleanly because for a given mass, data within any subset of reaction time and photon energy can be extracted to test and cross check a hypothesis.

C. Sensitivity

It is useful to have a quantitative measure of the sensitivity of the apparatus when considering feasibility of an experiment. In this discussion we consider collecting data at a single photon energy E, summing the events observed over a single peak in the mass spectrum. We denote $S_i(E)$ as the ion counts per time bin in an experiment for species i ionized at photon energy E:

$$S_i(E) = N_i\left[\frac{r_p^2}{4x^2}\right]\sigma_i(E)d_{beam}n_{ph}\Delta t_{bin}\tau_{ms}\Phi_{\text{det}}C\sqrt{\frac{m_i}{m_{He}}} \qquad (2)$$

where N_i is the density of the neutral species in the reactor tube, r_p the radius of the pinhole, x the distance along the molecular beam from the pinhole to the point of ionization, $\sigma_i(E)$ the photoionization cross section, d_beam the width of the molecular beam in the direction of the VUV propagation from which ions are collected, n_ph the number of ionizing photons s^{-1}, Δt_bin the temporal width of each time bin, τ_ms the mass spectrometer transmission, Φ_det the detection efficiency of ions incident on the detector, C the number of cycles (laser pulses) averaged, and m_i the mass of the detected species.

The term in square brackets in Eq. 2 is the fractional decrease in density of species i at a distance x downstream from the pinhole.[23] This expression is accurate to within 1% for purely effusive flow when $x > 8r_\text{p}$, as is the case in our instrument. Because the actual flow is not purely effusive, the term in brackets is a lower limit to the true fractional density at distance x.

The final term is the square root of the ratio of the mass of the detected species to that of the bath gas, helium. This mass discrimination factor has been discussed by Hsu and Tung.[24] They measured its value in a similar sampling configuration and confirmed that heavier species are more concentrated on the centerline of the expansion in proportion to the square root of their mass. Our mass spectra of the standard calibration mixture mentioned in section III.A lead to the same conclusion. It appears there is no *a priori* derivation of this relationship due to the complicated nature of expansions that are intermediate between effusive and supersonic.

For a practical example, Fig. 6 shows the time profile of acetone photodissociated at λ = 193 nm for 5000 laser pulses. The raw data is binned with Δt_{bin} = 25 μs. The acetone density in the reactor of $N = 7.9 \times 10^{12}$ cm^{-3} in 4 Torr of helium at 298 K corresponds to an acetone mole fraction of 6.2×10^{-5}. Other parameters required by Eq. 2 are given in the caption to Fig. 6. The calculated pre-laser value of S_{58}(10.2 eV) = 3818 counts bin^{-1}, compares favorably to the measured signal of 1062 ± 33 counts bin^{-1}. We attribute the discrepancy in these values to inaccuracy in our estimates of τ_{ms}, Φ_{det}, and n_{ph}.

Because our apparatus counts single ions, the random uncertainty is governed by Poisson statistics, where the standard deviation is related to the mean by $\sigma = \mu^{0.5}$. Therefore, a useful approach for utilizing Eq. 2 is to decide what signal-to-noise ratio is required, for example $S/N = 20 = S_i(E)^{0.5}$, which can be achieved with $S_i(E)$ = 400 counts timebin^{-1}. Equation 2 can be solved for N_i, giving the minimum density of species *i* that will yield the required signal-to-noise ratio. Combining constants yields the practical equation:[25]

$$N_i = 1.89 \times 10^6 (\text{amu}^{1/2}\text{cm}^{-1}) \frac{S_i(E)}{\sigma_i(E) n_{ph} \Delta t_{bin} C \sqrt{m_i}} \quad (3)$$

We commonly use coarser temporal binning than in Fig. 6, usually Δt_{bin} = 250 μs. Under these conditions, for a typical mass 58 amu molecule, with $\sigma = 10^{-17}$ cm^2 at a photon flux n_{ph} = 5 x 10^{13} s^{-1} and 10 minutes of signal averaging at a 4 Hz laser repetition rate, S/N = 10 timebin^{-1} requires N_i = 8.3 x 10^{10} cm^{-3}. At 4 Torr total pressure and 298 K, this density represents a mole fraction of 6.5 x 10^{-7}, a value that emphasizes the need for ultrapure helium as the main carrier gas.

When the focus of an experiment is on the identification of isomeric composition, rather than extraction of quantitative rate coefficients, the acquired time profiles may be used simply to distinguish photolysis products, primary reaction products, secondary reaction products, and impurities. In these cases the sensitivity of the experiment is often much higher than indicated by Eq. 3, because one may integrate over a long time range when extracting an (E, m/z) image, from which PIE curves are extracted. In this case, Δt_{bin} in Eq. 3 may be replaced by the total integration time. Using the parameters of the previous example, but with a typical integration of 80 ms of reaction time, the same S/N = 10 can be achieved in only 1 minute of signal averaging at a much lower molecular density of N_i = 2.6 x 10^9 cm^{-3}.

D. Temporal instrument response function

As discussed in section II.D, the 20 MHz oscillator that determines the "timestamp" of each recorded ion limits the temporal resolution of the detection system to 50 ns. This resolution is more than sufficient for our purposes because the gas dynamics of the

expansion imposes the fundamental limit on the fastest kinetic signal we can measure. Taatjes,[26] building on earlier work of Moore and Carr,[27] has examined the effect of the molecular velocity distribution on the determination of rate coefficients in time-resolved mass spectrometry.

The kinetic traces we obtain are a convolution of the true species temporal profiles with the instrument response function. If we could ionize neutral molecules inside the pinhole of the reactor tube, and transport the ions instantaneously (and without collisions) to the mass spectrometer, the true temporal profile of the species would be measured. In reality, the point of ionization is 2.5 cm downstream from the pinhole, resulting in two effects on the temporal response function.

Consider a group of neutral molecules in the reactor tube with identical initial positions immediately in front of the pinhole at some time t_1. The concentration of these molecules [C(t_1)] is the desired observable. Because the ionization point is 2.5 cm from the pinhole, there will be a time delay before this packet of molecules reaches the ionization region. If each molecule had the same velocity u along the centerline of the expansion, the propagation delay $t_d = x/u$ would simply shift the observed kinetic profile, but not distort its shape. In reality, there is a spread in velocities Δu among the group of molecules, such that the information [C(t_1)] is both delayed by the finite mean velocity, and blurred by the velocity distribution such that $\Delta t_d = x/\Delta u$. These two effects are the dominant contributions to our instrument response function.

It follows that in designing the instrument, the distance x between pinhole and ionization should be made as small as possible. Furthermore, harder supersonic expansions in the lightest possible carrier gas decrease both t_d and Δt_d because of the

higher mean velocity and the smaller velocity spread in supersonic beams. For these reasons our experiments are always conducted in a large excess of helium. Increasing the pressure in the reactor moves the expansion closer to the supersonic limit, but the maximum pressure in our configuration is set at ~ 10 Torr based on the considerations of radial diffusion discussed in section II.A.

In the limit of a purely effusive expansion, the mean velocity of helium at 298 K is u = 1255 m s^{-1}, whereas that for acetone is 330 m s^{-1}, corresponding to delay times t_d = 20 and 76 μs, respectively. In effusive sampling, the full width spread in arrival time Δt_d is on the same order as t_d, and Taatjes[26] and Carr[27] give a rule of thumb that systematic errors in measuring a first-order rate coefficient k will be essentially negligible if $k\Delta t_d <$ 0.1. For mass 58 (e.g., acetone) this rule suggests that reaction conditions should be adjusted so that $k < 1300$ s^{-1}. In the supersonic limit, the heavier molecules adopt the same mean speed as the carrier gas; in this case t_d doesn't depend on mass and is smaller than in the effusive limit.

Examining Fig. 6b provides some indication of the actual instrument response function. The photodissociation of acetone at 193 nm occurs on a picosecond timescale, and therefore the depletion of acetone in our apparatus would have a true transition time of ~ 20 ns, reflecting the pulse width of the excimer laser. This timescale is comparable to the inherent time resolution of the detector and electronics, but is orders of magnitude faster than the gas dynamics timescales discussed above, which will therefore limit the overall response time. In Fig. 6b, the photolysis laser fires at 20.000 ms. The acetone signal falls halfway to its final value in ~ 50 μs. The instrument response time is

therefore not much larger than 50 μs, in agreement with the calculation above for mass 58 (acetone) in a purely effusive source.

The apparatus should be able to measure first order rate coefficients with good fidelity for $k < 2000$ s^{-1}. The lower limit for rate coefficient measurements is usually set by the rate at which the radical under study undergoes first-order loss on the walls of the reactor. This value varies with each species and particular coating of the reactor, but is typically in the range of $3 < k_{wall} < 30$ s^{-1}. For example, in the self reaction of allyl radicals (C_3H_5), we measure $k_{wall} = 13$ s^{-1} while measuring the apparent pseudo first-order rate coefficient $k' = k[C_3H_5]_0$ over the range 60 – 640 s^{-1}.[28]

E. Quantitative determination of isomer fractions

In this section we give a brief example of the quantitative determination of isomer ratios. Figure 7 shows a measurement of a known mixture of C_3H_4 isomers that is comprised of 28% allene (H_2CCCH_2) and 72% propyne ($HCCCH_3$). Allene has an IE of 9.692 eV with a gradual onset, whereas propyne has an IE of 10.36 eV with an abrupt onset, as demonstrated by their respective PIE curves plotted in Fig. 7. From the observed signal $S(E)$ at $m/z = 40$, we can quantify the mole fractions X_i of each isomer in the mixture if we know the absolute photoionization efficiency curves[29,30] $\sigma_i(E)$ of each isomer. We fit the data to the following equation:

$$S(E) \propto \sigma_{total}(E) = \sum_{i=1}^{m} \sigma_i(E) X_i \qquad (4)$$

where the $\sigma_i(E)$ act as basis functions for each of m isomers. In the case of Fig. 7, the best fit yields a measurement of 30% allene and 70% propyne. Note that allene (the

isomer with the lower IE) can be detected independently of propyne for $E < 10.36$ eV, but propyne may not be detected independently of allene.

IV. CONCLUSIONS

We have constructed a multiplexed time- and photon-energy–resolved photoionization mass spectrometer for the study of the kinetics of gas phase, neutral chemical reactions. When quasi-continuous, tunable VUV synchrotron radiation is used for photoionization, the apparatus produces a 3-dimensional data cube $S(m/z, t, E)$ from which 2-D images and 1-D profiles of the data may be extracted. This highly multiplexed approach provides new insights into reaction mechanisms, reduces the effect of systematic errors, and enables valuable cross checks in the interpretation of data.

In addition to the mass selectivity inherent in mass spectrometry, the apparatus enables resolution of different structural isomers by measuring photoionization efficiency curves. This capability of probing isomer-resolved chemical kinetics simultaneously for all species in a reaction system holds great promise for the study of contemporary problems in reaction mechanisms.

ACKNOWLEDGMENTS

We thank Dr. Mahadeva Sinha (Jet Propulsion Laboratory) and Intelligent Ion Inc. for technical advice in optimizing the mass spectrometer for photoionization, and Prof. Evan Williams (University of California, Berkeley) for helpful discussions. We thank Mr. Eric Granlund (University of California, Berkeley) for excellent machining of custom parts, Dr. Oswald Siegmund (Sensor Sciences) for assistance in implementing the detector technology, and Dr. Kevin Wilson (Lawrence Berkeley National Laboratory) for advice

and support at the Chemical Dynamics Beamline. This work is supported by the Division of Chemical Sciences, Geosciences, and Biosciences, the Office of Basic Energy Sciences, the U.S. Department of Energy. Sandia is a multiprogram laboratory operated by Sandia Corporation, a Lockheed Martin Company, for the National Nuclear Security Administration under Contract DE-AC04-94-AL85000. The Advanced Light Source is supported by the Director, Office of Science, Office of Basic Energy Sciences, of the U.S. Department of Energy under Contract No. DE-AC02-05CH11231 at Lawrence Berkeley National Laboratory.

REFERENCES

[1] Wilhelmy, L. F. Annalen der Physik und Chemie **81**, 413 (1850).

[2] G. Porter, Proc. Roy. Soc. (London) Ser. A **200**, 284 (1950).

[3] The phenomenal success of gas chromatography / mass spectrometry instruments applied to analysis of complex chemical mixtures relies on chemical separation (by chromatography) into pure components followed by 70 eV electron bombardment mass spectrometry. This powerful technique is nevertheless unsuitable for our purposes due to its slow time response.

[4] G. Capozza, E. Segoloni, F. Leonori, G. G. Volpi, and P. Casavecchia, J. Chem. Phys. **120**, 4557 (2004).

[5] I. R. Slagle, F. Yamada, and D. Gutman, J. Am. Chem. Soc. **103**, 149 (1981).

[6] I. R. Slagle and D. Gutman, J. Am. Chem. Soc. **107**, 5342 (1985).

[7] C. Fockenberg, H. J. Bernstein, G. E. Hall, J. T. Muckerman, J. M. Preses, T. J. Sears, and R. E. Weston, Jr., Rev. Sci. Instrum. **70**, 3259 (1999).

[8] M. A. Blitz, A. Goddard, T. Ingham, and M. J. Pilling, Rev. Sci. Instrum. **78**, 034103 (2007).

[9] M. P. Sinha and M. Wadsworth, Rev. Sci. Instrum. **76**, 025103 (2005).

[10] J. Mattauch, Phys. Rev. **50**, 617 (1936).

[11] C. A. Taatjes, N. Hansen, D. L. Osborn, K. Kohse-Hoeinghaus, T. A. Cool, and P. R. Westmoreland, Phys. Chem. Chem. Phys. **9**, 1 (2007).

[12] G. Meloni, P. Zou, S. J. Klippenstein, M. Ahmed, S. R. Leone, C. A. Taatjes, and D. L. Osborn, J. Am. Chem. Soc. **128**, 13559 (2006).

[13] F. Goulay, D. L. Osborn, C. A. Taatjes, P. Zou, G. Meloni, and S. R. Leone, Phys. Chem. Chem. Phys. **9**, 4291 (2007).

[14] G. Meloni, T. M. Selby, F. Goulay, S. R. Leone, D. L. Osborn, and C. A. Taatjes, J. Am. Chem. Soc. **129**, 14019 (2007)

[15] C. J. Howard, J. Phys. Chem. **83**, 3 (1979).

[16] J. Brunning and L. J. Stief, J. Chem. Phys. **84**, 4371 (1986).

[17] P. A. Heimann, M. Koike, C. W. Hsu, D. Blank, X. M. Yang, A. G. Suits, Y. T. Lee, M. Evans, C. Y. Ng, C. Flaim, and H. A. Padmore, Rev. Sci Instrum. **68**, 1945 (1997).

[18] Vallerga, J. V.; Siegmund, O. H. W. *Nucl.* Inst. Methods Phys. Res. A **2000**, *442*, 159.

[19] D. W. Minsek and P. Chen, J. Phys. Chem. **94**, 8399 (1990).

[20] T. Zhang, X. N. Tang, K. C. Lau, C. Y. Ng, C. Nicolas, D. S. Peterka, M. Ahmed, M. L. Morton, B. Ruscic, R. Yang, L. X. Wei, C. Q. Huang, B. Yang, J. Wang, L. S. Shen, Y. W. Zhang, and F. Qi, J. Chem. Phys. **124**, 074302 (2006).

[21] D. L. Osborn, P. Zou, T. M. Selby, F. Goulay, G. Meloni, A. Fahr, and C. A. Taatjes, in preparation.

[22] F. Goulay, A. J. Trevitt, G. Meloni, T. M. Selby, D. L. Osborn, C. A. Taatjes, and S. R. Leone, J. Am. Chem. Soc. (submitted).

[23] W. M. Howard, Phys. of Fluids **4**, 521 (1961).

[24] W. L. Hsu and D. M. Tung, Rev. Sci. Instrum. **63**, 4138 (1992).

[25] Units used in this equation are the same as in Fig. 5.

[26] C. A. Taatjes, Int. J. Chem. Kinet. **39**, 565 (2007).

[27] S. B. Moore and R. W. Carr, Int. J. Mass Spectrom. Ion Phys. **24**, 161 (1977).

[28] T. M. Selby, G. Meloni, F. Goulay, S. R. Leone, A. Fahr, C. A. Taatjes, and D. L. Osborn, J. Phys. Chem. A (submitted).

[29] G. R. Ho, M. S. Lin, Y. L. Wang, and T. W. Change, J. Chem. Phys. **109**, 5868 (1998)

[30] D. M. P. Holland and D. A. Shaw, Chem. Phys. **243**, 333 (1999).

Figure Captions

1) Cross section view of the multiplexed photoionization mass spectrometer.
2) Cross section view of the reactor tube, mass spectrometer, and detector region. A) pinhole, B) ion optics, C) electrostatic sector, D) magnetic sector, E) 2-dimensional time- and position-sensitive detector, F) partition wall dividing the ionization region from the detection region for the purposes of differential pumping, G) pumping ports for the ionization region, H) pumping port for the detector region.
3) Schematic of the ion detector and the data acquisition system. Components of the system: (D) extra delay to ensure stop always follows start, (A) fast analog amplifier, (CFD) constant fraction discriminator, (TDC) time to digital converter, (TS) timestamping board, (DMA) dynamic memory access data acquisition card.
4) Time-independent mass spectrum of a dilute C_2H_4 / C_3H_6 mixture. A) 2-D spatial image of ion positions on the detector. The *y* axis is linear in physical space, whereas the *x* axis has been transformed so that it is linear in *m*/*z* ratio. B) Corrected spatial ion image (see text), C) 1-D mass spectra corresponding to panels A and B.
5) Representation of a 3-dimensional data cube. Three orthogonal 2-D slices are shown as images, along with 1-D profiles extracted from these images.
6) Time profile of $m/z = 58$ ions observed in the photolysis of acetone. A) Complete profile. The increase of signal beginning at $t = 100$ ms is due to pump out of the irradiated gases. B) Response near the laser pulse at $t = 20.00$ ms. The conditions in this graph are: $E = 10.2$ eV, $N_{acetone} = 7.9 \times 10^{12}$ cm^{-3}, $r_p = 325$ μm, $x = 2.5$ cm,

σ(10.2 eV) = 10.8 x 10^{-18} cm^2, d_{beam} = 0.5 cm, n_{ph} = 9 x 10^{13} s^{-1}, Δt_{bin} = 25 x 10^{-6} s, τ_{ms} = 0.1, Φ_{det} = 0.5, C = 5000 laser pulses, m = 58 amu.

7) PIE curve of a known mixture of C_3H_4 isomers. Dashed lines show basis functions (PIE curves of pure isomers). Solid line is the best fit using Eq. 4.

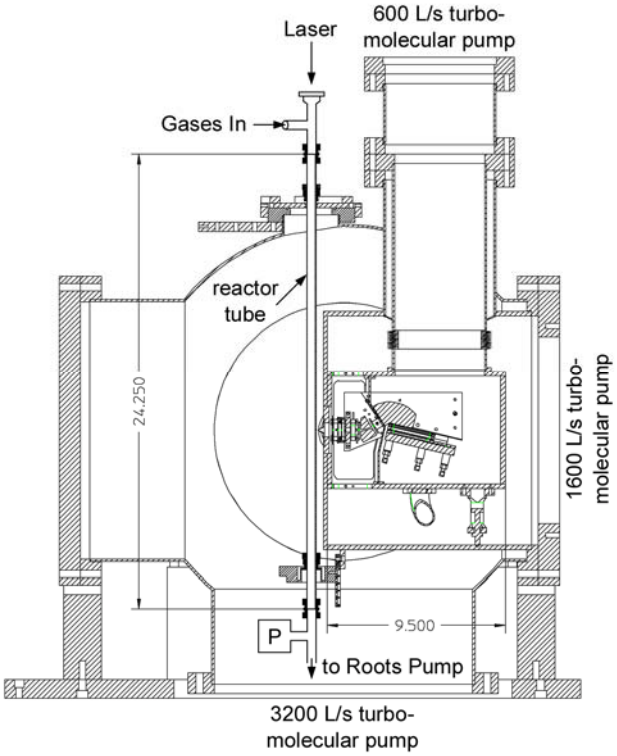

Fig. 1, Osborn et al.

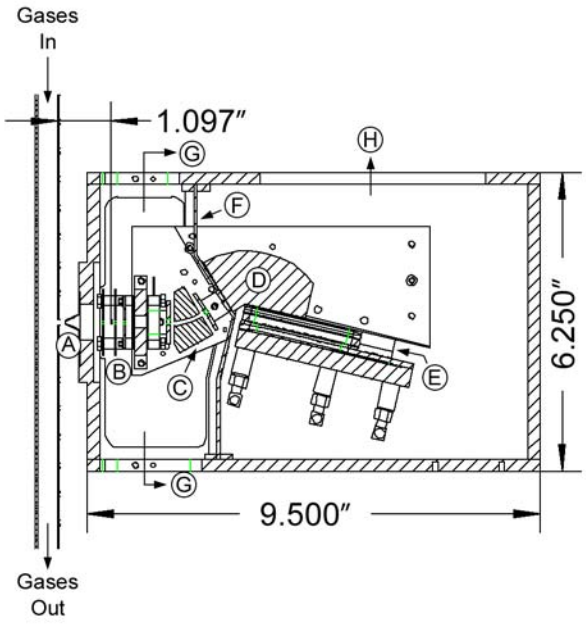

Fig. 2, Osborn et al.

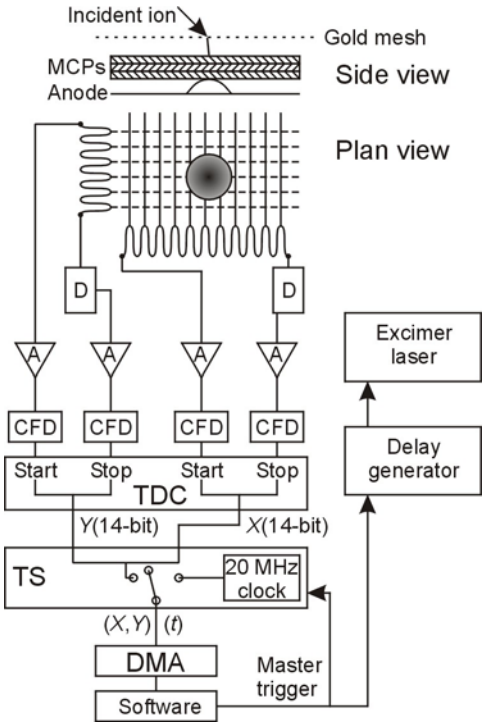

Fig. 3, Osborn et al.

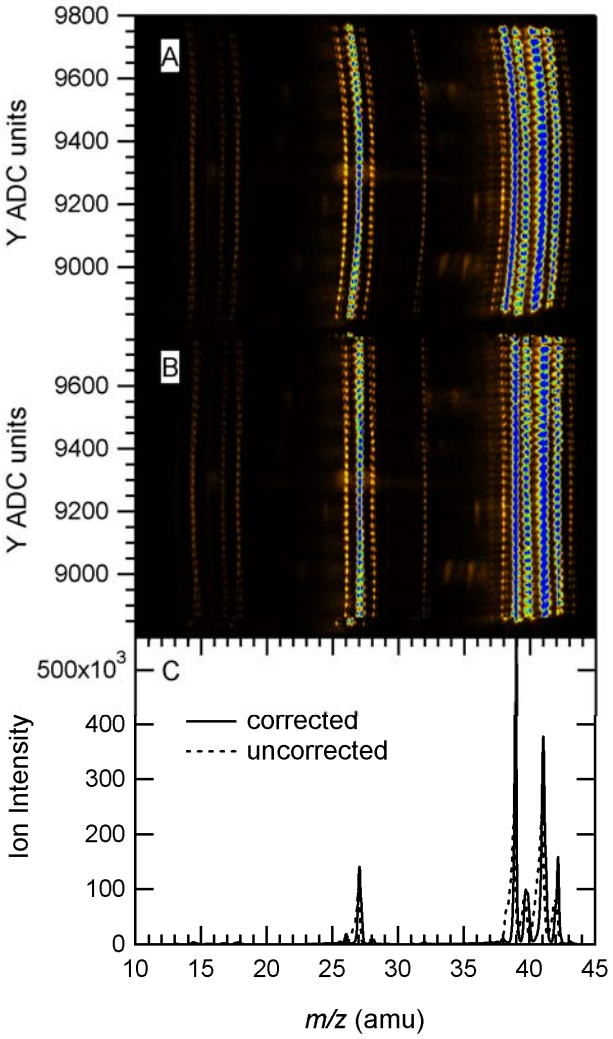

Fig. 4, Osborn et al.

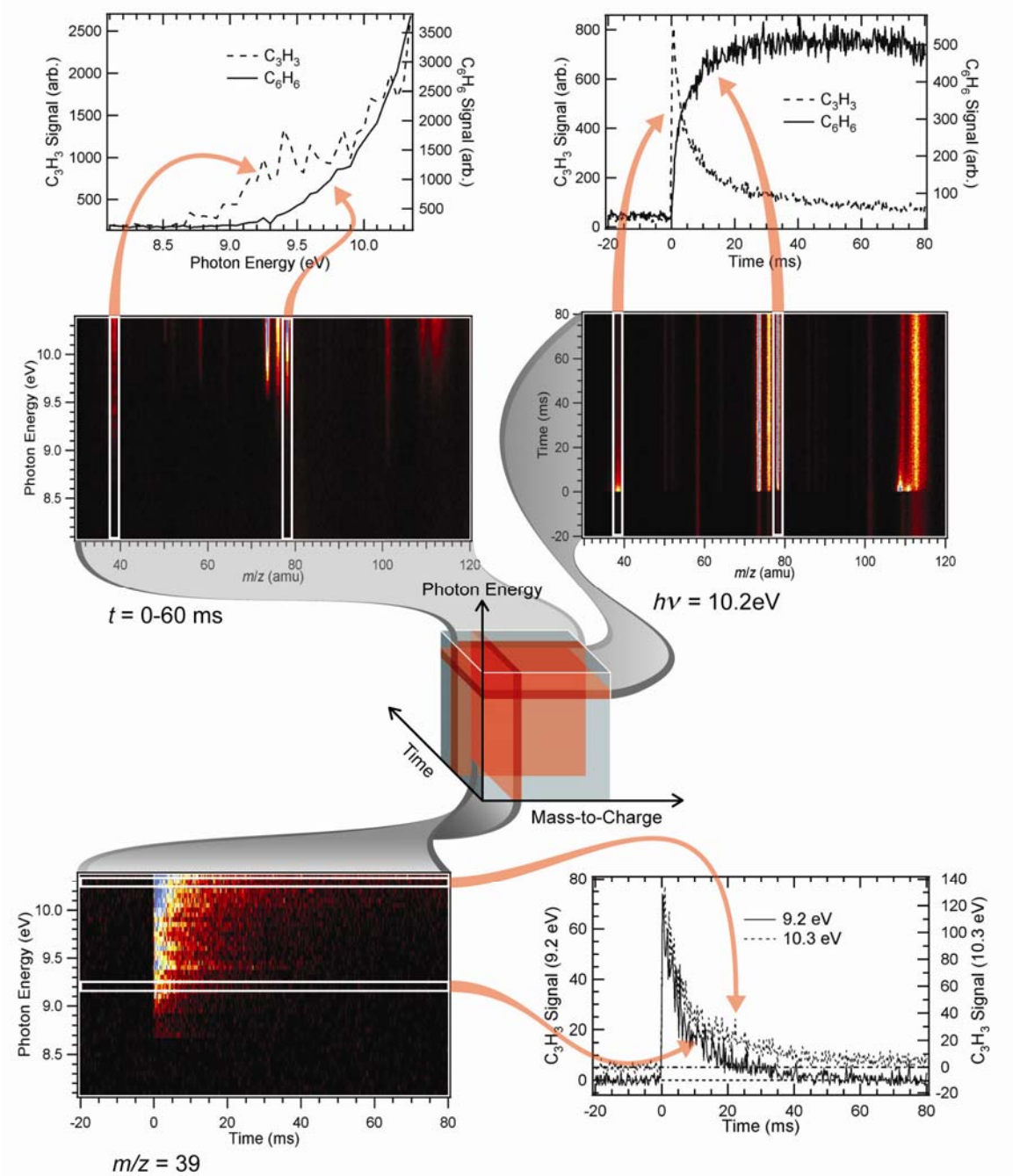

Fig. 5, Osborn et al.

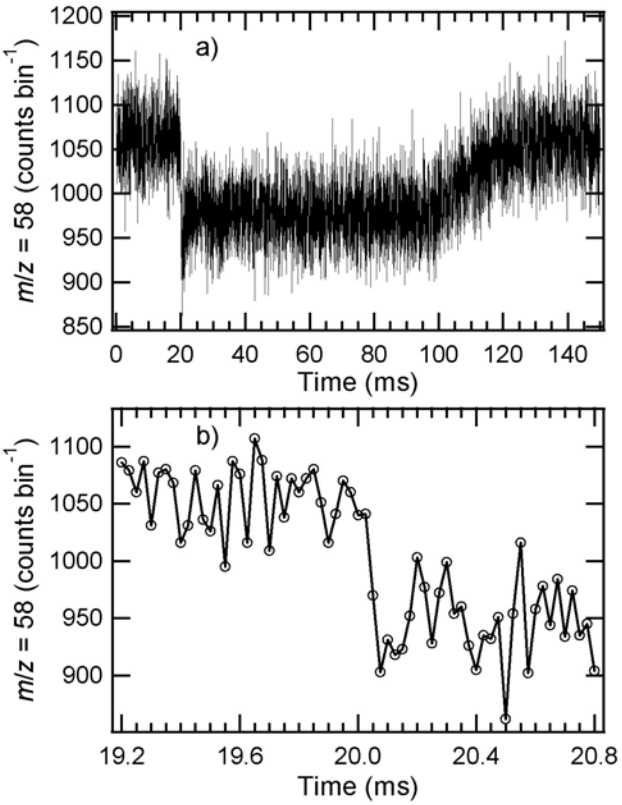

Fig. 6, Osborn et al.

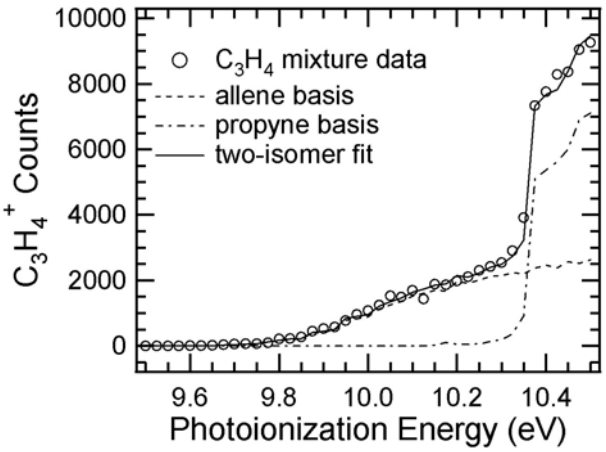

Fig. 7, Osborn et al.